Nanoparticle Size Effects in Cobalt Ferrite Electrodes for Magnetic-Field-Assisted Water Electrolysis

Viviana B. Daboin[a], Julieta S. Riva[a], Paula G. Bercoff[b]*,

[a] CONICET, Instituto de Investigaciones en Fisicoquímica de Córdoba (INFIQC). Universidad Nacional de Córdoba, Facultad de Ciencias Químicas, Ciudad Universitaria, X5000HUA Córdoba, Argentina.

[b] CONICET, Instituto de Física Enrique Gaviola (IFEG). Universidad Nacional de Córdoba, Facultad de Matemática, Astronomía, Física y Computación, Ciudad Universitaria, X5000HUA Córdoba, Argentina.

* paula.bercoff@unc.edu.ar

Keywords: $CoFe_2O_4$ nanoparticles, oxygen evolution reaction, magnetic-field-enhanced electrocatalysis, spin polarization, Langmuir-Blodgett films.

Abstract

We investigate the role of nanoparticle size and magnetic properties in magnetically assisted oxygen evolution reaction (OER) using $CoFe_2O_4$ nanoparticle-based anodes assembled on Indium Tin Oxide (ITO) substrates via the Langmuir–Blodgett technique. $CoFe_2O_4$ nanoparticles synthesized by thermal decomposition (TD) and self-combustion (SC) routes yield small (~12 nm) and large (~83 nm) single-domain ferrimagnetic particles, respectively. This strategy enables a systematic comparison of size-dependent structural, magnetic, and electrocatalytic properties under external magnetic fields. Nanoparticles prepared by TD form more compact, homogeneous films that exhibit higher intrinsic OER activity due to improved surface coverage and charge-transfer efficiency. However, their lower saturation magnetization, attributed to surface spin disorder, limits the magnitude of magnetic-field-induced enhancement. In contrast, nanofilms composed of SC nanoparticles display weaker intrinsic catalytic activity but higher saturation magnetization, resulting in a stronger OER enhancement under an applied magnetic field, consistent with a more effective field-driven spin alignment. Measurements under a 1.30 kOe field reveal increased catalytic activity for both systems, with greater enhancement when the field is applied parallel to the substrate. This arises from the combined effects of spin polarization and Lorentz-force-induced mass transport, being the latter active only when the field is perpendicular to the current flow. These findings highlight the need to balance nanoparticle size, film morphology, and magnetic properties to optimize magnetically assisted OER electrocatalysts.

1. Introduction

The continuously increasing global energy demand, coupled with escalating environmental degradation, makes the development of efficient and sustainable energy conversion and storage technologies imperative. Among the available approaches, electrochemical water splitting powered by electricity represents a highly promising strategy for storing excess renewable energy in the form of hydrogen [1,2]. This technology involves two kinetically sluggish half-reactions: the hydrogen evolution reaction (HER), which occurs at the cathode, and the oxygen evolution reaction (OER), which occurs at the anode .

In particular, the overall efficiency of water splitting is largely limited by the OER, as it involves a high activation energy, complex multi-electron and proton transfer processes that demand high overpotentials. Consequently, the development of efficient electrocatalysts is essential to accelerate this reaction. Although noble-metal-based catalysts, such as RuO_2 and IrO_2, currently exhibit excellent OER performance, their high cost and limited availability severely hinder large-scale and sustainable implementation. Therefore, the design of cost-effective, chemically stable, and highly active OER electrocatalysts remains a critical challenge for advancing water-splitting technologies.

Among electrocatalysts for water splitting, cobalt ferrite ($CoFe_2O_4$) has emerged as a promising candidate due to its low cost and high catalytic activity. Cobalt-based catalysts are particularly attractive because the incorporation of additional metals into their lattice can significantly enhance their electrocatalytic performance. Cobalt spinel oxides exhibit high chemical stability and efficient charge-transport properties, making them suitable platforms for the development of inexpensive and readily available electrocatalysts. In particular, $CoFe_2O_4$ with a partially inverted spinel structure has been extensively investigated as an OER catalyst, and its activity can be further tuned through strategies such as hybridization, morphology control, and particle size engineering [2].

One novel strategy to improve OER kinetics involves applying an external magnetic field during electrolysis. Previous studies have proposed that the observed performance enhancement arises mainly from indirect effects, such as improved mass transport driven by Lorentz-force-induced convection or local heating generated by high-frequency alternating magnetic fields. However, this improvement may also be associated with spin-polarization effects. Since O-O bond formation requires spin conservation to produce molecular oxygen in its paramagnetic triplet ground state, spin polarization at the catalyst surface could promote parallel spin alignment of oxygen intermediates, thereby enhancing reaction efficiency [3, 4].

Garcés-Pineda *et al*. have recently demonstrated a direct enhancement of electrocatalytic OER under a magnetic field and attributed this effect to changes in the magnetic properties of the catalysts (ferromagnetic or antiferromagnetic) [3]. Similarly, Ren *et al.* showed that OER enhancement occurs with ferromagnetic catalysts but not with non-ferromagnetic ones, linking this behavior to spin polarization during the first electron-transfer step. This spin-dependent charge transfer facilitates the formation of triplet-state O_2, highlighting the role of spin-polarized kinetics in OER and providing guidelines for the design of spin-dependent electrocatalysts [5].

Furthermore, Davis *et al.* studied different materials, for Co_3O_4, $CoFe_2O_4$, and Fe_3O_4, and concluded that the cobalt/iron ratio is an important parameter for the OER reactivity of the films, while the surface morphology plays only a minor role. Also they studied structure-reactivity correlations in thin-film electrocatalysts exposing (001) and (111) facets. The (001) facet was more active in Co_3O_4, whereas the (111) facet showed higher activity in $CoFe_2O_4$ and Fe_3O_4. Tafel analysis revealed lower slopes for the (001) facets and for iron-containing films [6,7]. Besides, Ge *et al.* showed that the intrinsic activity of a single-domain catalyst is higher than that of a multi-domain counterpart [8].

As it has been demonstrated, the intrinsic magnetic properties of cobalt ferrite strongly depend on its morphology and crystalline structure, which are in turn governed by the synthesis method. Among the commonly used synthesis approaches are the thermal decomposition (TD) and the self-combustion (SC) methods. Thermal decomposition is widely used to produce spherical, highly monodisperse $CoFe_2O_4$ nanoparticles stabilized by organic ligands, with morphology and size controlled by precursors, surfactants, and reaction conditions. Commonly employed metal acetylacetonates and surfactants such as oleylamine and oleic acid allow the formation of nanospheres, nanocubes, and nanohexagons, although this method typically involves complex procedures, costly precursors, and limited scalability [9, 10]. In contrast, the self-combustion method offers a low-cost, rapid, and scalable alternative, using organic fuels such as urea, glycine, or citric acid to drive exothermic reactions between metal nitrates and fuels at elevated temperatures, enabling the large-scale synthesis of metal oxide nanoparticles [10-12].

In our previous work, we investigated the magnetic characteristics of nanofilms based on $CoFe_2O_4$ nanoparticles synthesized by TD and SC routes. Both synthesis methods render crystalline nanoparticles, being the obtained by SC bigger in size, with higher saturation magnetization and effective anisotropy constant K_{eff} values. In this work, we investigate the use of $CoFe_2O_4$ nanoparticles synthesized by TD or SC methods and deposited onto conductive glass substrates as anodes for the OER [10]. The Langmuir Blodgett method was used to fabricate homogeneous and stable anodes from hydrophobic nanoparticles [13]. Then, we systematically examine the influence of an externally applied magnetic field during the reaction, focusing on how the magnetic properties of the nanoparticles and the resulting nanofilms affect magnetically assisted OER catalysis.

2. Materials and methods

2.1 Synthesis of $CoFe_2O_4$ nanoparticles

2.1.1 Thermal decomposition route

$CoFe_2O_4$ nanoparticles were synthesized by a thermal decomposition method adapted from previously reported procedures [9, 10]. Briefly, 2 mmol of $Fe(acac)_3$, 1 mmol of $Co(acac)_2$, 10 mmol of hexadecanediol, 6 mmol of oleic acid (OA), and 6 mmol of oleylamine were mixed with 20 mL of benzyl ether in a three-neck flask. The reaction mixture was magnetically stirred under a nitrogen atmosphere for 60 min at room temperature. Subsequently, the temperature was increased to 100 °C and maintained for 30 min to remove residual moisture. The mixture was then heated to 200 °C for 30 min to initiate nucleation, followed by a further increase to 280 °C for 60 min to promote particle growth.

After cooling to room temperature, ethanol was added to precipitate the nanoparticles, which were collected magnetically and washed several times with ethanol. The resulting powder was dried at 60 °C overnight. As obtained, the nanoparticles were already coated with oleic acid as a direct outcome of the synthetic procedure, and were labeled **Co-TD**.

2.1.2 Self-combustion route

$CoFe_2O_4$ nanoparticles were also obtained by a self-combustion synthesis following a procedure from references [10-12]. CoC_2O_4, $Fe(NO_3)_3$, and citric acid were used as precursors without further purification. First, cobalt oxalate and ferric nitrate were dissolved in 50 mL of water to achieve a total metal concentration of 1 M ([Fe(III)] + [Co(II)]). Then, 50 mL of a 3 M citric acid solution were added, and the mixture was heated at 40 °C for 30 min under vigorous stirring. Slow evaporation produced a viscous gel, which, upon heating below 200 °C, underwent a self-propagating combustion process that yielded a powder. The resulting material was calcined at 800 °C for 2 h.

To improve dispersibility, 0.15 g of the obtained powder was dispersed in a mixture of 25 mL of absolute ethanol and 0.075 g of stearic acid. The suspension was sonicated at 80 °C for 1 h, washed five times to remove unbound stearic acid, and dried at 60 °C for 24 h. The surface-modified nanoparticles were labeled **Co-SC**.

2.2 Preparation of $CoFe_2O_4$ nanoparticle films

Nanofilms based on Co-TD and Co-SC nanoparticles were prepared using the Langmuir–Blodgett (LB) technique, following general procedures previously reported for ferrite nanoparticle monolayers [10, 13]. The nanoparticles were spread at the air/water (Milli-Q, 18.2 MΩ·cm) interface from chloroform-based dispersions, allowing the solvent to evaporate prior to compression. Surface pressure was monitored with a Wilhelmy plate using a KSV NIMA LB trough (model 2000).

Co-TD nanofilms were prepared using a 1.5 $mg \cdot mL^{-1}$ dispersion, from which 150 µL was spread onto the water surface. After solvent evaporation, the monolayer was compressed at 10 $mm \cdot min^{-1}$ and transferred onto pre-cleaned Indium Tin Oxide (ITO) substrates at a surface pressure of 40 $mN \cdot m^{-1}$ using a vertical dipping speed of 3 $mm \cdot min^{-1}$. Co-SC nanofilms were assembled under the same experimental conditions, except that a 5 $mg \cdot mL^{-1}$ dispersion was employed and 300 µL was spread at the interface. All substrates were previously cleaned with acetone, ethanol, and water.

2.3 Experimental Techniques

The structural, morphological, and magnetic properties of the Co-TD and Co-SC nanoparticles and their corresponding nanofilms were characterized using different techniques. The crystal structure was examined by X-ray powder diffraction (XRD) using a PANalytical X'Pert Pro diffractometer equipped with Cu Kα radiation (λ = 1.5418 Å). Diffraction patterns were collected over the 2θ range of 10°–80° with a step size of 0.02°. Morphological analysis was performed by field-emission scanning electron microscopy (FE-SEM, Zeiss Sigma), and transmission electron microscopy (TEM, Zeiss Leo 906E) operated at an accelerating voltage of 110 kV. Magnetic measurements were performed at 300 K using a Cryogenic Ltd. vibrating sample magnetometer (VSM) under applied magnetic fields up to ±50 kOe. $CoFe_2O_4$ nanoparticles were measured in the form of thin pressed disks, whereas the nanofilms were characterized directly on their substrates. For the films, the external magnetic field was applied both parallel (**in-plane, IP**) and perpendicular (**out-of-plane, OoP**) to the film surface in order to assess possible magnetic anisotropy. In all cases, the magnetic response of the bare substrate was subtracted from the nanofilm data. The magnetic parameters

reported for the nanofilms were obtained from the substrate-corrected M(H) curves. To express the magnetic response in emu·g^{-1}, the magnetic moment of each nanofilm was normalized using the saturation magnetization of the corresponding nanoparticle powder measured under the same experimental conditions.

2.4 Electrochemical measurements

The electrocatalytic performance of the Co-TD and Co-SC nanofilms was evaluated in a conventional three-electrode configuration using a CHI 760C electrochemical workstation. The ITO-coated glass substrates containing the films were used directly as working electrodes. A platinum foil served as the counter electrode, while an Ag/AgCl (sat. KCl) electrode was employed as the reference.

All measurements were performed in 0.1 M KOH aqueous solution (pH = 13). The potentials were converted to the reversible hydrogen electrode (RHE) scale according to: $E_{RHE} = E_{Ag/AgCl} + 0.059 \times pH + 0.197$ V. The overpotential (η) was calculated as: $\eta\,(V) = E_{RHE} - 1.23$ V.

Polarization curves were recorded by linear sweep voltammetry (LSV) at a scan rate of 5 mV·s^{-1}, and current densities were normalized to the geometric area of the electrode. All electrochemical measurements were performed in triplicate using independently prepared electrodes. Tafel slopes were extracted by fitting the LSV data to the Tafel equation: $\eta = a + b \log j$, where b is the Tafel slope and j is the current density. The fitting was performed over the linear region of the Tafel plots, within an overpotential range of 0.4–0.7 V. Electrochemical impedance spectroscopy (EIS) was performed at 1.7 V vs RHE over a frequency range of 0.01 Hz to 1000 Hz with an amplitude of 5 mV. The impedance spectra were fitted using a Randles equivalent circuit consisting of the solution resistance (Rs) in series with a parallel combination of a constant phase element (CPE) and the charge-transfer resistance (Rct). The resulting spectra were fitted using ZPLOT/ZVIEW software (Scribner Associates Inc.).

To evaluate the influence of an external magnetic field on the electrocatalytic response, the measurements were repeated under a constant magnetic field of 1.30 kOe, applied both in-plane (IP) or out-of-plane (OoP) with respect to the film surface, as schematized in Figure 1. The scheme also depicts the electrochemical configuration employed for all experiments. The magnetic field intensity was verified prior to each measurement using a handheld digital teslameter (TD8620).

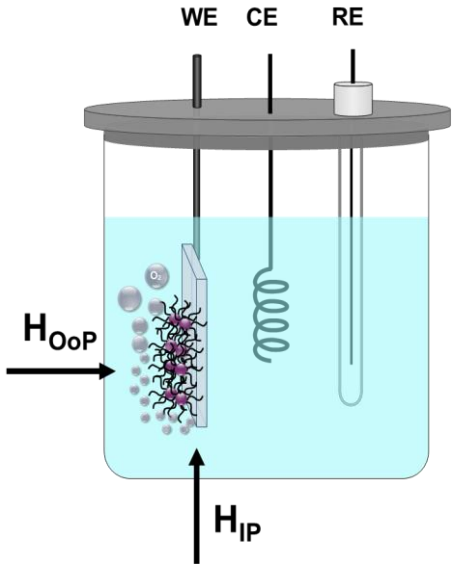

Figure 1. Illustration of the electrochemical cell used for OER measurements with $CoFe_2O_4$ nanoparticle-modified electrodes under external magnetic field stimulation. The magnetic field is applied either parallel (IP) or perpendicular (OoP) to the electrode surface.

3. Results

3.1 Nanoparticle characterization

Figure 2 summarizes the structural and magnetic characterization of the Co-TD and Co-SC nanoparticles. The TEM images shown in Figure 2(a) for Co-TD and Figure 2(b) for Co-SC reveal that both samples consist of nanoparticles that deviate from perfect sphericity, exhibiting well-defined faceted morphologies instead. The corresponding particle-size distributions shown in Figures 2(c) and 2(d) were fitted using a log-normal function, yielding average diameters of (12 ± 1) nm for Co-TD and (83 ± 2) nm for Co-SC, in agreement with the particle dimensions typically reported for thermal-decomposition and combustion routes, respectively.

The XRD patterns of both samples (Figure 2(e)) show reflections characteristic of the cubic spinel phase of $CoFe_2O_4$ (JCPDS 22-1086, also displayed in Figure 2(e)), with no secondary phases detected. Crystallite sizes estimated from the Scherrer equation are (9 ± 2)

nm for Co-TD and (80 ± 5) nm for Co-SC, matching well with the TEM-estimated particle sizes and indicating that both kinds of nanoparticles are essentially single-crystalline. As expected, sample Co-TD exhibits broader diffraction peaks due to its smaller crystallite size.

The hysteresis loops of Co-TD and Co-SC nanoparticles were measured at 300 K in the form of thin compacted disks, with maximum applied fields of ±50 kOe, which were enough to saturate the samples. Figure 2(d) shows the data in the field region of H < ±10 kOe , for the sake of clarity. Both samples exhibit ferrimagnetic behavior with well-defined remanence and coercivity. The saturation magnetization (*Ms*) reaches 84 emu·g^{-1} for Co-SC (close to the reported bulk values of cobalt ferrite [14]), whereas Co-TD displays a significantly lower *Ms* of 33 emu·g^{-1}. This reduction is attributed to the much smaller size of the Co-TD nanoparticles, where increased surface spin disorder and a high surface-to-volume ratio hinder complete spin alignment at the particle boundaries [15].

The coercive fields follow the same decreasing trend for the smaller NPs: 1.05 kOe for Co-SC and 0.65 kOe for Co-TD. This difference reflects the well-known size dependence of coercivity, whereby as the particle size approaches the critical diameter (D_C), the coercivity increases, reaches a maximum, and subsequently decreases toward the superparamagnetic regime, with decreasing size [16]. In the present case, both samples remain within the single-domain regime, meaning that magnetization reversal requires overcoming the full anisotropy energy barrier [17], which leads to an appreciable coercivity even for the smaller Co-TD nanoparticles. A more detailed analysis of the magnetic properties has been reported previously [10], and a concise summary is included in the Supplementary Information.

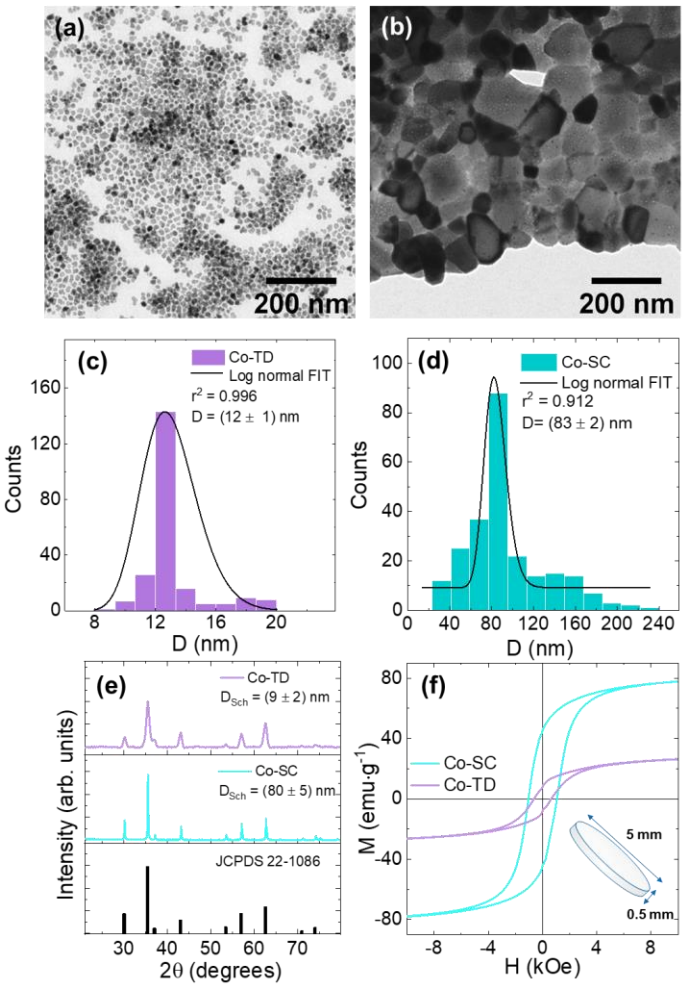

Figure 2. Bright-field TEM images of (a) Co-TD and (b) Co-SC nanoparticles. The corresponding particle-size histograms, together with the fitting curves used to determine the average particle size distributions, are shown below each micrograph. (c) X-ray diffraction patterns of Co-TD and Co-SC nanoparticles, together with the JCPDS reference pattern used to index the reflections of the spinel structure. (d) Room-temperature hysteresis loops of Co-TD and Co-SC nanoparticles. Maximum applied fields of ±50 kOe were used, although only the region corresponding to H < 10 kOe is shown for clarity. The inset schematizes the shape and dimensions of the compacted pellets used for the magnetic measurements.

3.2 Nanofilm Assembly and Characterization

Surface pressure-area isotherms were recorded for the Co-TD and Co-SC nanoparticle monolayers to determine suitable transfer conditions onto solid substrates, using the Langmuir-Blodgett technique (as described in **Section 2.2**). A detailed analysis of the isotherm features for both nanoparticle systems, including phase behavior and compression regimes, has been reported previously [10]. Based on those results, a surface pressure of 40 $mN \cdot m^{-1}$ was selected for the deposition of the nanofilms.

Using these optimized conditions, the nanoparticles were transferred to ITO substrates by vertical dipping in a Langmuir–Blodgett trough. With both nanoparticles, the procedure yielded homogeneous coatings, confirming the efficient transfer of the nanoparticle monolayers onto the substrates. Representative SEM images of the resulting nanofilms are shown in Figures 3(a) and 3(b).

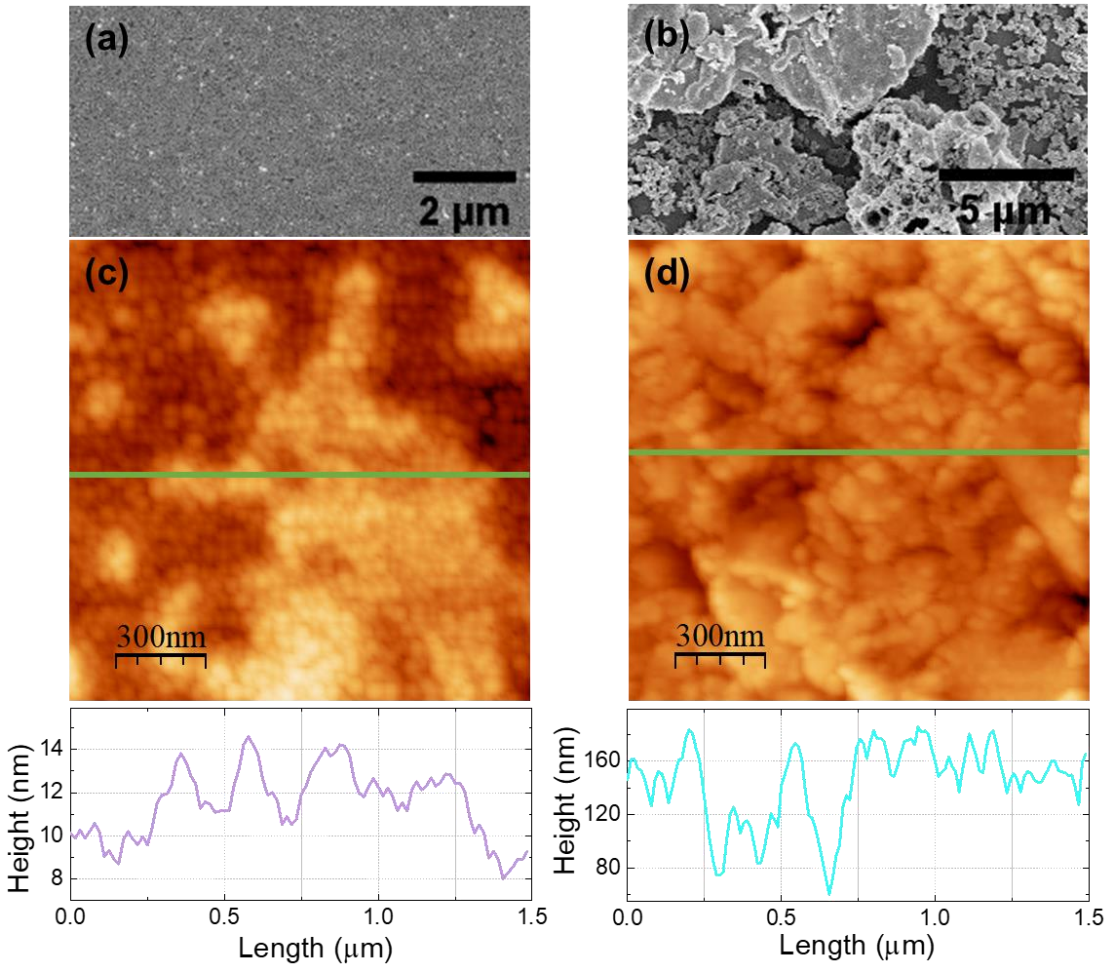

Figure 3. SEM images of (a) Co-TD and (b) Co-SC nanofilms, showing an effective coverage of the substrate in both cases. AFM topography images of (c) Co-TD and (d) Co-SC nanofilms with the corresponding line profiles at the bottom.

These images reveal continuous nanoparticle coverage across the substrate, although Co-SC films exhibit a more granular texture due to the larger particle size, whereas Co-TD films appear smoother and more compact, consistent with the smaller nanoparticles. Figures 3(c) and 3(d) show AFM topographic images of the nanofilms, confirming that Co-TD nanoparticles self-assemble in a more ordered distribution, likely due to their smaller size, rendering a more uniform and thinner film. Cross-sectional profiles extracted from several AFM images revealed average film thicknesses of approximately 12 nm for Co-TD and 160 nm for Co-

SC. Furthermore, the Langmuir-Blodgett transfer ratios were 1.0 ± 0.1 and 0.9 ± 0.1 for Co-TD and Co-SC, respectively, indicating an efficient and reproducible transfer of the nanoparticle layers onto the ITO substrates.

Figure 4(a) shows the room-temperature hysteresis loops of the Co-SC and Co-TD nanofilms measured with the magnetic field applied both parallel (IP) and perpendicular (OoP) to the film plane, as schematically illustrated in Figure 4(b). The loops are displayed after subtracting the magnetic contribution of the substrate. In both samples, a ferrimagnetic behavior is observed together with a clear anisotropy, indicating a preferred in-plane magnetic alignment.

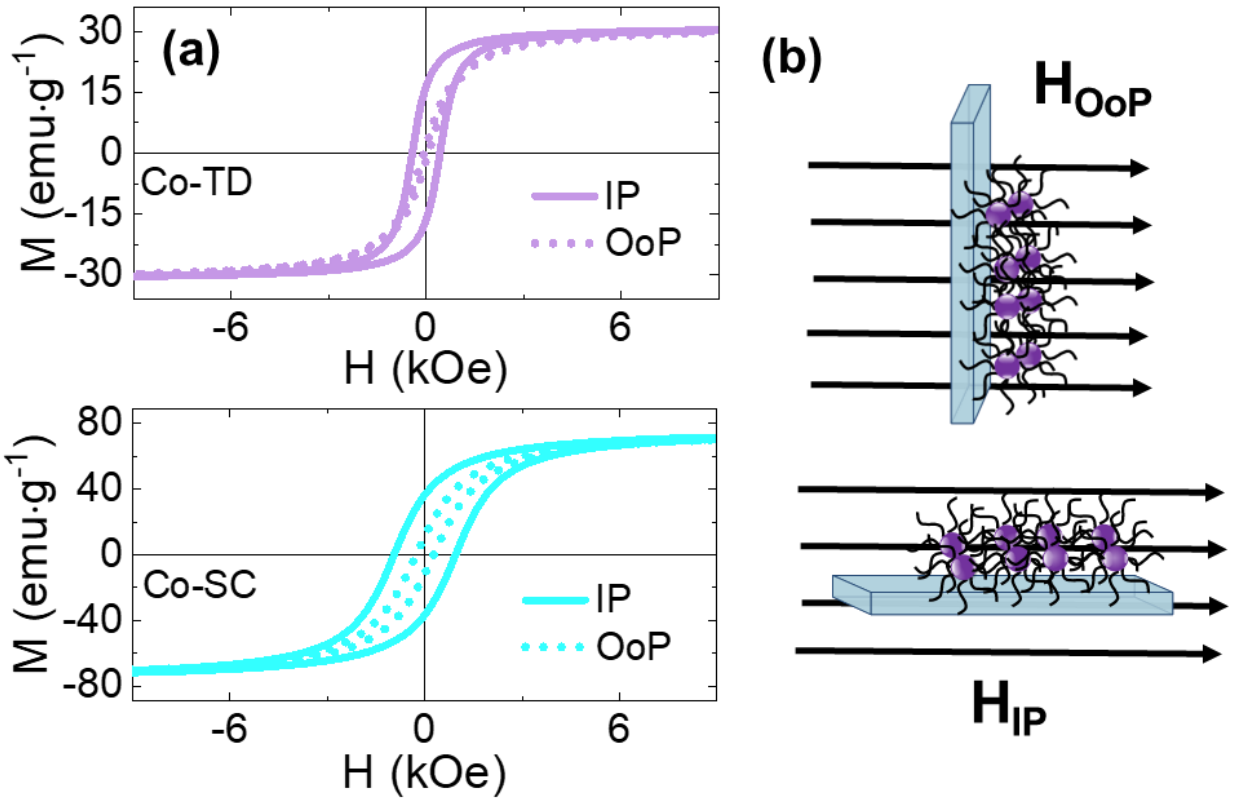

Figure 4. (a) Hysteresis loops of the nanofilms measured at room temperature, with the field applied in plane (IP) and out of plane (OoP), as schematized in (b). Maximum applied fields of ±50 kOe were applied, but only the region of H< ±10 kOe is displayed, for clarity.

Quantitatively, the Co-SC nanofilm reaches a saturation magnetization of 84 emu·g^{-1}, while Co-TD attains 33 emu·g^{-1}. These results are consistent with the bulk-like response of the larger Co-SC nanoparticles and the reduced magnetic moment associated with the smaller Co-TD particles. The remanent magnetization follows the same tendency, as listed in Table 1

The coercive fields also show a clear dependence on the field orientation for both nanofilms, with lower values when the magnetic field is applied in the out-of-plane configuration. This behavior reflects the dominant role of shape anisotropy, which favors magnetization lying within the plane of the films. All the relevant magnetic parameters are summarized in Table 1. A more detailed and extensive magnetic analysis of these nanofilms, including the determination of their effective anisotropy, is available in our previous publication [10], of which a brief summary can be found in the Supplementary Information.

Table 1. Magnetic parameters of the nanofilms: saturation magnetization (M_S), remanent magnetization (M_R), magnetization at 1.30 kOe obtained from the M(H) curves, and coercive field (H_C).

Sample	M_S (emu· g^{-1})	M_R (emu· g^{-1})		M(1.30 kOe) (emu· g^{-1})		*Hc* (Oe)	
		(IP)	(OoP)	(IP)	(OoP)	(IP)	(OoP)
Co-TD	33	17	2	28	20	430	70
Co-SC	84	43	22	56	46	1230	570

3.3 Effect of Magnetic Field on the OER Performance

Figure 5(a) shows the linear sweep voltammetry (LSV) curves of bare ITO and ITO coated with Co-TD and Co-SC nanofilms. As expected, the bare ITO electrode displays the lowest current densities, confirming its poor OER activity, while both cobalt ferrite nanofilms significantly enhance the response. Among them, the Co-TD film exhibits the highest current densities based on the geometric electrode area, with values consistently above those of Co-SC across the entire potential range. As an example, the current increase at 2.0 V is enhanced by (47±2)% with the Co-SC nanofilm, while it reaches (770 ± 9)% with the Co-TD nanofilm. The superior electrocatalytic performance observed for the Co-TD electrode may be attributed to its more uniform and homogeneous surface coverage. It should be noted, however, that the Co-TD and Co-SC electrodes differ in film thickness and morphology. Therefore, the comparison presented here reflects the overall performance of the assembled electrodes based on geometric-area-normalized current densities and should not be interpreted as a direct comparison of the intrinsic catalytic activity of the materials. It has been shown that the LB technique is particularly effective for NPs obtained by the TD method, primarily due to their smaller size and the fact that the synthesis procedure directly yields hydrophobic nanoparticles in a single step. In contrast, nanoparticles synthesized by the SC method require an additional surface-modification step to impart hydrophobicity prior to LB film fabrication.

The application of the magnetic field further increases the current in both samples, though with different intensities. At 2.0 V, the current density in Co-TD nanofilm increases by (50 ± 6) % in IP configuration and by (25 ± 4) % in OoP geometry, relative to 0 kOe (Figure 5(b)). Although Co-SC anode shows lower absolute currents, it displays a much stronger relative response to the magnetic field: at the same potential, the current rises by (260 ± 9) % in IP and (90 ± 7) % in OoP configurations (Figure 5(c)).

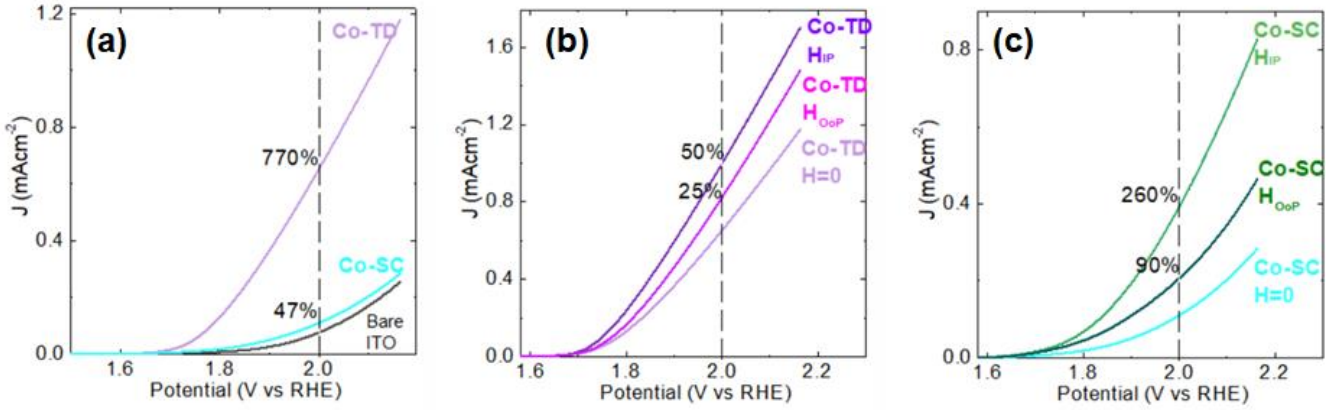

Figure 5. (a) Linear sweep voltammetry (LSV) curves of bare ITO and ITO electrodes coated with Co-TD and Co-SC nanofilms, recorded in 0.1 M KOH at a scan rate of 5 mV s^{-1}. (b) LSV curves of the Co-TD nanofilm measured

in the absence of a magnetic field (0 kOe) and under a 1.30 kOe magnetic field applied in the in-plane (IP) and out-of-plane (OoP) configurations. (c) LSV curves of the Co-SC nanofilm measured under the same conditions. All current densities are normalized to the geometric electrode area.

The reported values correspond to the average of three independent measurements, while the uncertainties reflect the experimental variability among replicates. In the out-of-plane (OoP) configuration, the electric current flows parallel to the applied magnetic field, resulting in a negligible Lorentz force. Therefore, the observed enhancement in catalytic activity in this case is consistent with a dominant contribution from spin-polarization effects, although other magnetic-field-induced phenomena cannot be completely excluded. In contrast, in the in-plane (IP) configuration, the electric current is perpendicular to the magnetic field, allowing the Lorentz force to become operative and induce additional mass transport [18,19]. Consequently, the enhanced catalytic effect observed under the IP configuration arises from the combined influence of spin polarization and Lorentz-force-induced mass transport, the latter being active only in this geometry. The different mechanisms operating in the IP and OoP setups are illustrated in Figure 6(a).

This enhanced catalytic effect observed under a magnetic field applied in the IP direction correlates with reduced Tafel slopes and lower charge-transfer resistance, indicating improved reaction kinetics and interfacial charge transport (Table S1 and Figure S3 in the Supplementary Information). The Co-TD nanofilm exhibits a Tafel slope of (68 ± 5) mV·dec^{-1} at 0 kOe, which decreases to (60 ± 3) and (51 ± 2) mV·dec^{-1} under OoP and IP magnetic fields, respectively. Similarly, its charge-transfer resistance changes from 550 Ω at 0 kOe to 680 Ω (OoP) and 467 Ω (IP). For Co-SC, the Tafel slope decreases from (170 ± 8) mV·dec^{-1} to (162 ± 2) mV·dec^{-1} (OoP) and (138 ± 4) mV·dec^{-1} (IP), while the charge-transfer resistance changes from 934 Ω to 1680 Ω (OoP) and 760 Ω (IP). These results indicate that the magnetic field influences both the reaction kinetics and the interfacial charge-transfer process, with the IP configuration providing the most favorable conditions for OER performance.

Both nanofilms exhibit an increase in current under the magnetic field, even more when it is applied in the IP configuration, and the effect is significantly more pronounced for Co-SC, suggesting a more effective enhancement process in this case. This stronger response correlates with its higher magnetization at 1.30 kOe (56 emu·g^{-1} in IP and 46 emu·g^{-1} in OoP), compared with Co-TD (28 emu·g^{-1} and 19 emu·g^{-1}, respectively), as obtained from their magnetization curves and summarized in Table 1. These magnetization differences indicate that Co-SC undergoes a more effective field-induced alignment, which likely contributes to the stronger enhancement of its OER current, as it is schematized in Figure 6(b). The electrochemical stability of both nanofilms was further evaluated by accelerated cycling and chronoamperometric measurements.

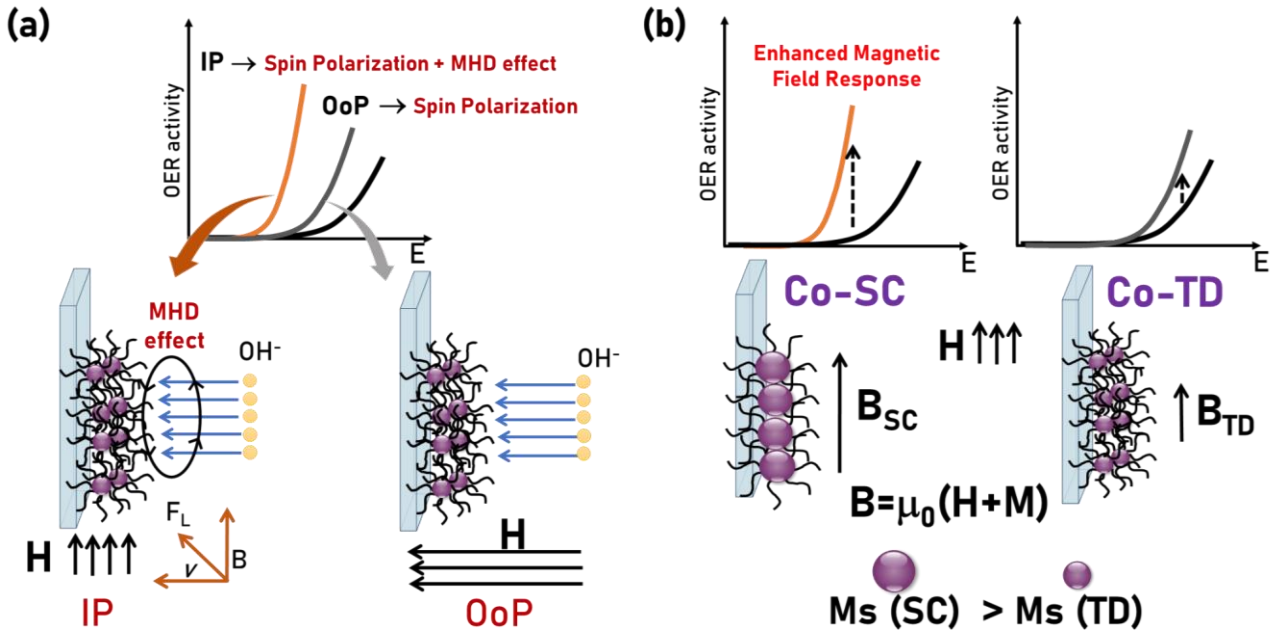

Figure 6. (a) Schematic illustration of the mechanisms that may contribute to the magnetic-field-enhanced OER performance, depending on the orientation of the external magnetic field. B_{SC} (B_{TD}) is the magnetic flux and *Ms*(SC) (*Ms*TD)) is the saturation magnetization corresponding to Co-SC (Co-TD) nanofilm. In the in-plane (IP) configuration, both spin polarization and magnetohydrodynamic (MHD) effects associated with Lorentz-force-induced mass transport may contribute to the electrocatalytic enhancement. In the out-of-plane (OoP) configuration, the Lorentz force is expected to be strongly suppressed, making the observed enhancement consistent with a dominant contribution from spin polarization. (b) Schematic representation of the nanoparticle-size effect on the magnetic-field-induced enhancement of the OER activity.

The electrochemical stability of both nanofilms was further evaluated by comparing LSV curves recorded before and after 400 electrochemical cycles, as well as by chronoamperometric measurements. The results, presented in the Supplementary Information (Figure S4), indicate that both nanofilms retain their electrocatalytic performance and exhibit good stability under the investigated OER conditions.

Conclusion

In this work, we studied the influence of nanoparticle size, magnetic properties, and external magnetic fields on the OER performance of $CoFe_2O_4$ nanoparticle-based anodes. By comparing nanofilms assembled from small nanoparticles synthesized by thermal decomposition and larger nanoparticles obtained via self-combustion methods, we demonstrate that particle size plays a dual role in determining the catalytic behavior. Smaller nanoparticles yield more homogeneous and compact Langmuir-Blodgett films, which enhance intrinsic OER activity through improved surface coverage, higher exposed active area, and more efficient charge transfer. However, their reduced saturation magnetization, arising from surface spin disorder, limits their ability to benefit from magnetic-field-assisted enhancement. Conversely, nanofilms composed of larger nanoparticles exhibit lower intrinsic OER activity but show a substantially stronger response to an applied magnetic field, due to their higher magnetization and more effective field-induced spin alignment. In both systems, the application of an in-plane magnetic field leads to a greater enhancement of OER activity than an out-of-plane field, consistent with the coexistence of spin-polarized reaction kinetics and Lorentz-force-induced mass transport, the latter being active only when the magnetic field is perpendicular to the current flow.

Overall, these results reveal that magnetically assisted

OER performance is maximized by a compromise between nanoparticle size and magnetic moment. The optimal electrocatalyst design should therefore combine small nanoparticles, to ensure uniform film formation and high intrinsic activity, with sufficiently strong magnetic properties to fully exploit spin polarization effects under an external magnetic field.

This study provides fundamental insights into the size-magnetism-reactivity relationship in ferrite-based electrocatalysts and offers clear guidelines for the development of advanced magnetically responsive OER electrodes.

Acknowledgements

This work was supported by ANPCyT-FONCyT (PICT-2020–0984), Secyt-UNC, and Conicet projects. Viviana Daboin acknowledges a doctoral fellowship from Conicet. We thank the 'Laboratorio de Análisis de Materiales por Espectrometría de Rayos X' (LAMARX-FAMAF-UNC, https://lamarx.famaf.unc.edu.ar) for granting access to their facilities.

Supplementary Information

1. Nanoparticle characterization

Figure S1 (a), (b) shows M vs. H loops measured between 5 K and 300 K for Co-TD and Co-SC nanoparticles, respectively. Both samples exhibit a clear ferrimagnetic behavior, with considerable values of remanence (M_R) and coercivity (H_C) over the entire temperature range.

A wasp-waisted hysteresis shape is observed in sample Co-SC at temperatures below 150 K, whereas this feature is absent in the other sample. Since XRD confirms the presence of a single crystalline phase, this behavior is attributed to the broad nanoparticle size distribution, as opposed to the quite narrow size distribution that the thermal decomposition method produces [10].

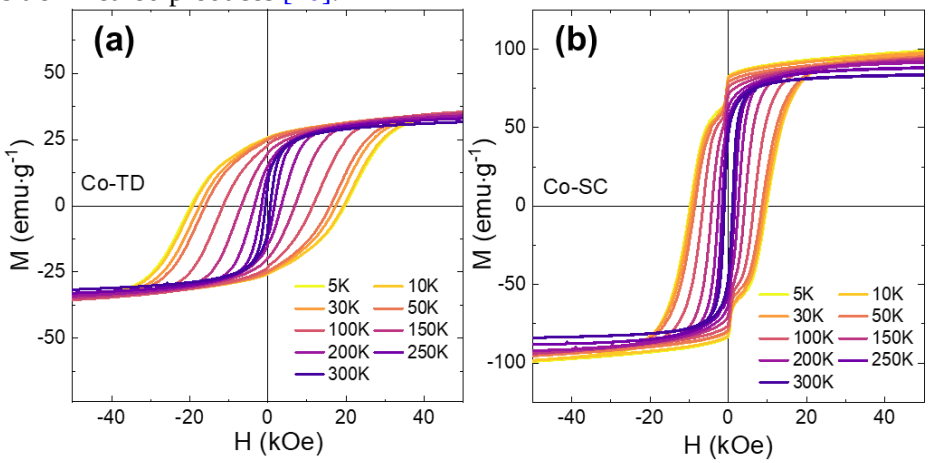

Figure S1. Hysteresis loops obtained at different temperatures of (a) Co-TD and (b) Co-SC nanoparticles.

2. Nanofilm Assembly and Characterization

Figure S2 (a) and Figure S2 (b) show in-plane M vs. H loops measured between 5 K and 300 K for Co-TD and Co-SC nanofilms, respectively, after subtracting the magnetic contribution from the substrate. In both samples, a steep increase in Ms with decreasing temperature can be noticed below 50 K, which is more evident in Co-TD nanofilm. This behavior can be ascribed to a spin-glass-like behavior, and it can be modeled considering the addition of a surface spin contribution to the modified Bloch law. A detailed analysis of this effect can be found in reference [10].

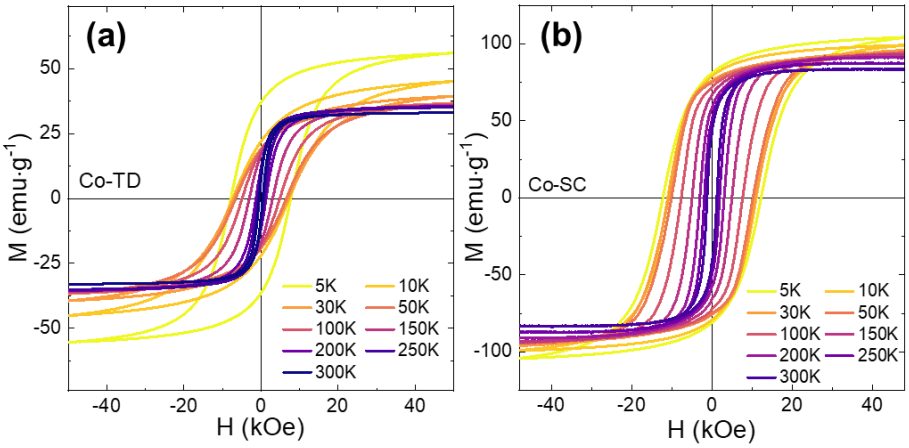

Figure S2. In-plane hysteresis loops recorded at different temperatures for nanofilms prepared from (a) Co-TD and (b) Co-SC nanoparticles.

3. Effect of Magnetic Field on the OER Performance

The analysis of the Tafel slopes (**Table S1**) further supports the trends observed in the LSV curves. As expected, bare ITO shows the poorest OER kinetics, with a slope of 187 mV·dec^{-1} at 0 kOe. Both cobalt ferrite nanofilms significantly improve this value, although with clear differences between them. The Co-TD film exhibits the lowest intrinsic slope (68 mV·dec^{-1} with H = 0 kOe), in line with its higher activity in the LSV curves. Under the magnetic field, the Tafel slope decreases to 51 mV·dec^{-1} in the IP configuration, indicating a further acceleration of the reaction kinetics, while the OoP value slightly increases to 83 mV·dec^{-1}, consistent with the smaller enhancement observed in the LSV response for this geometry.

Table S1. Tafel slopes for bare ITO and for the Co-TD and Co-SC nanofilms measured at 0 kOe and under a 1.30 kOe magnetic field in the in-plane (IP) and out-of-plane (OoP) configurations.

Tafel slope (mV·dec^{-1})			
Applied Field	**ITO+Co-TD**	**ITO+Co-SC**	**Bare ITO**
0 kOe	(68 ± 5)	(170 ± 8)	(187 ± 5)
OoP = 1.30 kOe	(60 ± 3)	(162 ± 2)	-
IP = 1.30 kOe	(51 ± 2)	(138 ± 4)	-

In contrast, the Co-SC nanofilm displays a much higher Tafel slope at 0 kOe (170 mV·dec^{-1}), confirming its poorer intrinsic kinetics compared with Co-TD. However, Co-SC is markedly more responsive to the magnetic field: the Tafel slope decreases to 138 mV·dec^{-1} in IP and to 162 mV·dec^{-1} in OoP, reflecting the same trend seen in the current increases from the LSV measurements. These reductions, although smaller than those of Co-TD in absolute terms, represent a larger relative improvement, which is consistent with the stronger magnetic-field-induced enhancement observed for this sample and with its higher magnetization values at 1.30 kOe.

The electrochemical impedance spectroscopy (EIS) results (**Figure S3(a)**) further corroborate the magnetic-field-dependent behavior of the two nanofilms. An inset in **Figure S3(a)** provides a magnified view of the high-frequency region, allowing a more clear comparison of the impedance response under the different magnetic field conditions. At 0 kOe, the charge-transfer resistance (Rct) follows the same order as the LSV and Tafel analyses: Co-TD shows the lowest value (550 Ω), followed by Co-SC (934 Ω), while bare ITO exhibits a much higher Rct

(4700 Ω), consistent with its poor electrocatalytic activity. When the magnetic field is applied in the IP configuration, Rct decreases to 467 Ω for Co–TD and to 760 Ω for Co-SC, indicating that magnetic alignment facilitates interfacial charge transfer in both samples. Conversely, the OoP field orientation increases the Rct of both films (680 Ω for Co-TD and 1680 Ω for Co-SC), suggesting that this configuration is less favorable for the electron-transfer process. The impedance data were fitted using a Randles equivalent circuit, schematically shown in **Figure S3 (b)**, which adequately describes the electrochemical response of the system. These results reinforce that the magnetic-field response of the ferrite films is strongly dependent on the field orientation, with the IP configuration providing the most efficient pathway for charge transfer during the OER.

Altogether, the combined analysis of the LSV curves (**Figure 4**), the Tafel slopes (**Table S1**), and the EIS-derived Rct values (**Figure S3 (a)**) confirms that Co-TD is intrinsically the most active nanofilm, but Co-SC exhibits a significantly stronger sensitivity to the applied magnetic field.

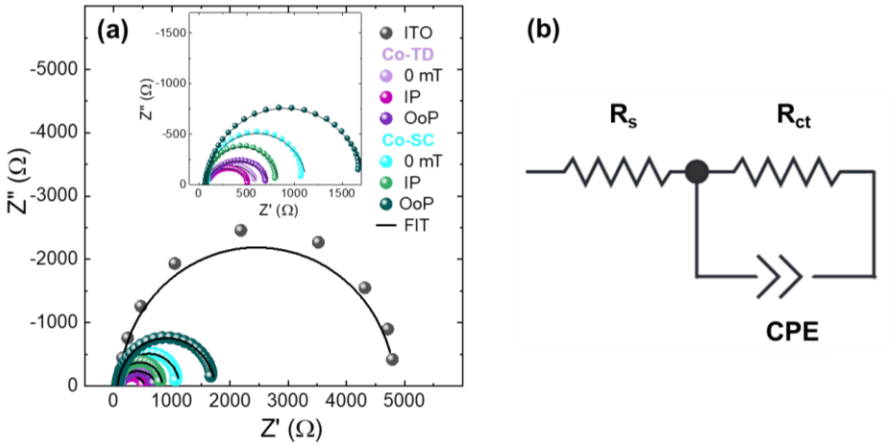

Figure S3. (a) Nyquist plots of bare ITO, Co-TD, and Co-SC nanofilms measured during the OER in 0.1 M KOH at a fixed potential, under 0 kOe and under a 1.30 kOe magnetic field applied in-plane (IP) and out-of-plane (OoP). The inset shows a magnified view of the high-frequency region. (b) Randles equivalent circuit used to fit the EIS data, where R_s represents the solution resistance, *CPE* the constant phase element associated with the double-layer capacitance, and R_{ct} the charge-transfer resistance.

4. Stability Tests

To evaluate the electrochemical stability of the Co-TD and Co-SC nanofilms under OER conditions, cyclic voltammetry tests and chronoamperometric measurements were performed. These experiments were carried out in the absence of an external magnetic field using the same electrochemical cell, electrolyte (0.1 M KOH), and experimental conditions employed for the electrocatalytic measurements described in the main text.

Figure S4 (a) compares the LSV curves recorded before and after 400 electrochemical cycles for both nanofilms. Only minor changes in the electrochemical response were observed, indicating that the films retain their electrocatalytic activity after prolonged cycling. In addition, chronoamperometric measurements performed at 1.96 V vs RHE for 5 h (**Figure S4 (b)**) showed only slight variations in the current density over time, demonstrating good operational stability under OER conditions.

These results suggest that the nanofilms remain firmly attached to the ITO substrate and do not undergo significant degradation during the electrochemical measurements.

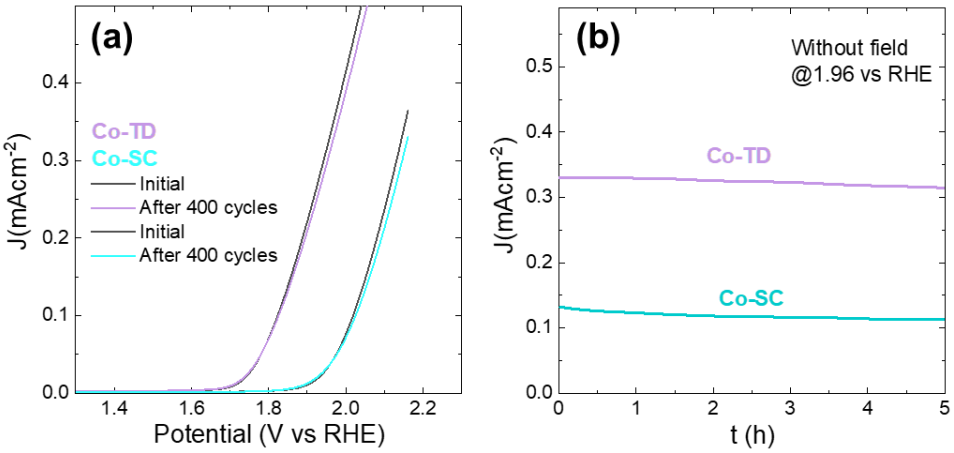

Figure S4. Stability assessment of Co-TD and Co-SC nanofilms under OER conditions. (a) Linear sweep voltammetry curves recorded before and after 400 electrochemical cycles. (b) Chronoamperometric response measured at 1.96 V vs RHE for 5 h in 0.1 M KOH.

References

[1] G.A. Gebreslase, M.V. Martínez-Huerta, D. Sebastián, M.J. Lázaro, Transformation of $CoFe_2O_4$ spinel structure into active and robust CoFe alloy/N-doped carbon electrocatalyst for oxygen evolution reaction, *J. Colloid Interface Sci.* 625 **(2022)** 70–82, https://doi.org/10.1016/j.jcis.2022.06.005.

[2] M. Afaq, M. Shahid, Iqbal Ahmad, Sheraz Yousaf, A. Alazmi, M.H.H. Mahmoud, I.H. El Azab, M.F. Warsi, Large-scale sonochemical fabrication of a Co_3O_4–$CoFe_2O_4$@MWCNT bifunctional electrocatalyst for enhanced OER/HER performances, *RSC Adv.* 13 **(2023)** 19046–19057. https://doi.org/10.1039/d3ra03117a.

[3] F.A. Garcés-Pineda, M. Blasco-Ahicart, D. Nieto-Castro, N. López, J.R. Galán-Mascarós, Direct magnetic enhancement of electrocatalytic water oxidation in alkaline media, *Nat. Energy* 4 **(2019)** 519–525. https://doi.org/10.1038/s41560-019-0404-4.

[4] A. Yu, T. Wu, X. Ren, Z.J. Xu, Spin-Promotion Effect to Oxygen Evolution Reaction, *Acc. Chem. Res*. 58 **(2025)** 3273−3280. https://doi.org/10.1021/acs.accounts.5c00510.

[5] X. Ren, T. Wu, Y. Sun, Y. Li, G. Xian, X. Liu, C. Shen, J. Gracia, H-J Gao, H- Yang, Z. J. Xu, Spin-polarized oxygen evolution reaction under magnetic field. *Nat Commun.* 12, 2608 **(2021)**. https://doi.org/10.1038/s41467-021-22865-y.

[6] E.M. Davis, A. Bergmann, C. Zhan, H. Kuhlenbeck, B.R. Cuenya, Comparative study of Co_3O_4(111), $CoFe_2O_4$(111), and Fe_3O_4(111) thin film electrocatalysts for the oxygen evolution reaction, *Nat Commun.* **(2023)** 14:4791. https://doi.org/10.1038/s41467-023-40461-0.

[7] E.M. Davis, A. Bergmann, H. Kuhlenbeck, B.R. Cuenya, Facet Dependence of the Oxygen Evolution Reaction on Co_3O_4, $CoFe_2O_4$, and Fe_3O_4 Epitaxial Film Electrocatalysts, *J. Am. Chem. Soc.* **(2024)** 146, 13770−13782, https://doi.org/10.1021/jacs.3c13595.

[8] J. Ge, X. Ren, R- Ruixi Chen, Y. Sun, T. Wu, S. Jun Hoong Ong, Z.J. Xu, Multi-Domain versus Single-Domain: A Magnetic Field is Not a Must for Promoting Spin-Polarized Water Oxidation, *Angew. Chem. Int. Ed.* 62 **(2023)** e202301721. https://doi.org/10.1002/anie.202301721.

[9] V. Daboin, S. Briceño, J. Suárez, G. Gonzalez, Effect of the dispersing agent on the structural and magnetic properties of $CoFe_2O_4/SiO_2$ nanocomposites, *J. Magn. Magn. Mater.* 451 **(2018)** 502–506. https://doi.org/10.1016/j.jmmm.2017.08.043.

[10] V. B. Daboin, J. S. Riva, P. G. Bercoff, Magnetic behavior of nanofilms prepared by assembling different Co ferrite nanoparticles, *Mater. Res. Bull.* 184 **(2025)** 113229. https://doi.org/10.1016/j.materresbull.2024.113229

[11] P. Bera, R. V. Lakshmi, B.H. Prakash, K. Tiwari, A. Shukla, A.K. Kundu, K. Biswas, H.C. Barshilia, Solution combustion synthesis, characterization, magnetic, and dielectric properties of $CoFe_2O_4$ and $Co_{0.5}M_{0.5}Fe_2O_4$ (M = Mn, Ni, and Zn), *Phys. Chem. Chem. Phys.* 22 **(2020)** 20087–20106. https://doi.org/10.1039/d0cp03161e.

[12] I. Haïk Dunn, S.E. Jacobo, P.G. Bercoff, Structural and magnetic influence of yttrium-for-iron substitution in cobalt ferrite, *J. Alloys Compd.* 691 **(2017)** 130–137. https://doi.org/10.1016/j.jallcom.2016.08.223.

[13] V.B. Daboin, J.S. Riva, P.G. Bercoff, Magnetic nanofilms prepared by Langmuir-Blodgett nanoarchitectonics using Co and Co-Y ferrite nanoparticles, *Mater. Res. Bull.* 189 **(2025)** 113449. https://doi.org/10.1016/j.materresbull.2025.113449.

[14] S.M. Ansari, R.D. Bhor, K.R. Pai, D. Sen, S. Mazumder, K. Ghosh, Y.D. Kolekar, C. V. Ramana, Cobalt nanoparticles for biomedical applications: Facile synthesis, physiochemical characterization, cytotoxicity behavior and biocompatibility, *Appl. Surf. Sci.* 414 **(2017)** 171–187. https://doi.org/10.1016/j.apsusc.2017.03.002.

[15] Z. Mahhouti, H. El Moussaoui, T. Mahfoud, M. Hamedoun, M. El Marssi, A. Lahmar, A. El Kenz, A. Benyoussef, Chemical synthesis and magnetic properties of monodisperse cobalt ferrite nanoparticles, *J. Mater. Sci. Mater. Electron.* 30 **(2019)** 14913–14922. https://doi.org/10.1007/s10854-019-01863-3.

[16] B.D. Cullity, C.D. Graham, *Introduction to Magnetic Materials*, 2nd ed., Wiley Online Library, **2008**. http://onlinelibrary.wiley.com/book/10.1002/9780470386323.

[17] A. Zorai, A. Souici, D. Dragoe, E. Rivière, S. Ouhenia, J. Belloni, M. Mostafavi. Superparamagnetic cobalt ferrite nanoparticles synthesized by gamma irradiation, *New J. Chem*. 47 **(2023)** 2626-2634. https://doi.org/10.1039/D2NJ05433G.

[18] V.B. Daboin, S.N. Moya Betancourt, E.D. Farias, J.S. Riva, P.G. Bercoff, Enhancement of the electrochemical oxygen evolution reaction by light and external magnetic fields, using hybrid electrodes made by Langmuir–Blodgett, *Electrochim. Acta* 480 **(2024)** 143910. https://doi.org/10.1016/j.electacta.2024.143910.

[19] K. Wang, Q. Yang, H. Zhang, M. Zhang, Hunan Jiang, Chen Zhenga, J. Li, Recent advances in catalyst design and activity enhancement induced by a magnetic field for electrocatalysis, *J. Mater. Chem. A* 11 **(2023)** 7802. https://doi.org/10.1039/D2TA09276J.